


Parametrically Activated Entangling Gates Using Transmon Qubits

S. A. Caldwell,^{*†} N. Didier,[†] C. A. Ryan,[†] E. A. Sete,[†] A. Hudson, P. Karalekas, R. Manenti, M. P. da Silva, R. Sinclair, E. Acala, N. Alidoust, J. Angeles, A. Bestwick, M. Block, B. Bloom, A. Bradley, C. Bui, L. Capelluto, R. Chilcott, J. Cordova, G. Crossman, M. Curtis, S. Deshpande, T. El Bouayadi, D. Girshovich, S. Hong, K. Kuang, M. Lenihan, T. Manning, A. Marchenkov, J. Marshall, R. Maydra, Y. Mohan, W. O'Brien, C. Osborn, J. Otterbach, A. Papageorge, J.-P. Paquette, M. Pelstring, A. Polloreno, G. Prawiroatmodjo, V. Rawat, M. Reagor, R. Renzas, N. Rubin, D. Russell, M. Rust, D. Scarabelli, M. Scheer, M. Selvanayagam, R. Smith, A. Staley, M. Suska, N. Tezak, D. C. Thompson, T.-W. To, M. Vahidpour, N. Vodrahalli, T. Whyland, K. Yadav, W. Zeng, and C. Rigetti

Rigetti Computing, 775 Heinz Avenue, Berkeley, California 94710, USA

 (Received 25 October 2017; revised manuscript received 30 March 2018; published 24 September 2018)

We describe and implement a family of entangling gates activated by radio-frequency flux modulation applied to a tunable transmon that is statically coupled to a neighboring transmon. The effect of this modulation is the resonant exchange of photons directly between levels of the two-transmon system, obviating the need for mediating qubits or resonator modes and allowing for the full utilization of all qubits in a scalable architecture. The resonance condition is selective in both the frequency and amplitude of modulation and thus alleviates frequency crowding. We demonstrate the use of three such resonances to produce entangling gates that enable universal quantum computation: one *i*SWAP gate and two distinct controlled-*Z* gates. We report interleaved randomized benchmarking results indicating gate error rates of 6% for the *i*SWAP (duration 135 ns) and 9% for the controlled-*Z* gates (durations 175 and 270 ns), limited largely by qubit coherence.

DOI: [10.1103/PhysRevApplied.10.034050](https://doi.org/10.1103/PhysRevApplied.10.034050)

A central challenge in building a scalable quantum computer with superconducting qubits is the execution of high-fidelity two-qubit gates within an architecture containing many resonant elements. As more elements are added, or as the multiplicity of couplings between elements is increased, the frequency space of the design becomes crowded and device performance suffers. In architectures composed of transmon qubits [1], there are two main approaches to implementing two-qubit gates. The first utilizes fixed-frequency qubits with static couplings where the two-qubit operations are activated by applying transverse microwave drives [2–8]. While fixed-frequency qubits generally have long coherence times, this architecture requires satisfying stringent constraints on qubit frequencies and anharmonicities [5,6,8], which requires some tunability to scale to many qubits [9]. The second approach relies on frequency-tunable transmons, and two-qubit gates are activated by tuning qubits into and out of resonance with a particular transition [10–16]. However, tunability comes at the cost of additional decoherence channels, thus significantly limiting coherence times [17]. In this approach the delivery of shaped unbalanced

control signals poses a challenge [15]. Such gates are furthermore sensitive to frequency crowding—avoiding unwanted crossings with neighboring qubit energy levels during gate operations limits the flexibility and connectivity of the architecture.

An alternative to these approaches is to modulate a circuit's couplings or energy levels at a frequency corresponding to the detuning between particular energy levels of interest [18–26]. This enables use of an entangling gate between a qubit and a single resonator [21,22], between a qubit and many resonator modes [26], between two transmon qubits coupled by a tunable mediating qubit [16,25], or between two tunable transmons coupled to a mediating resonator [23,24].

Building on these earlier results, we implement two entangling gates, *i*SWAP and controlled-*Z* (CZ), between a flux-tunable transmon and a fixed-frequency transmon. The gates are activated by modulating the tunable qubit in resonance with particular pairs of transmon states: $|10\rangle$ and $|01\rangle$ for the *i*SWAP gate and $|11\rangle$ and $|20\rangle$ (or $|02\rangle$) for the CZ gate. This direct qubit-qubit interaction provides each maximally entangling operation in a single step, without sacrificing any qubits to a mediating role. The interaction is a first-order process with an effective strength of roughly half the qubit-qubit coupling, and the resonance conditions depend on both the frequency and amplitude of

^{*}caldwell.shane@gmail.com

[†]These authors contributed equally.

modulation. The availability of a second dimension in the control space, combined with the selectivity of the resonances, mitigates the effect of frequency crowding in architectures where each qubit has many neighbors. The modulation amplitude can be used to vary the frequency spectrum of the resonances, and up to three entangling gates, per neighbor, can be realized at each amplitude. The ability to apply both *i*SWAP and CZ gates between pairs of qubits may reduce circuit complexity, as these operations are not locally equivalent. However, the *i*SWAP gate is locally equivalent to a CNOT gate followed by the interchange of the qubit labels [27]. Both the *i*SWAP and the CZ gates are universal for quantum computation when combined with local operations on the individual qubits [27,28].

Our experimental results are obtained with the circuit shown in Fig. 1(a). This circuit comprises a fixed-frequency transmon (*F*) and a tunable transmon (*T*), coupled capacitively with a strength *g*. The tunable transmon, based on an asymmetric superconducting quantum interference device (SQUID), has a first transition frequency ω_T that depends on the externally applied flux bias Φ as shown in Fig. 1(e). We modulate ω_T by applying a flux bias of the form

$$\Phi(t) = \bar{\Phi} + \tilde{\Phi} \cos(\omega_p t + \theta_p), \quad (1)$$

with static bias $\bar{\Phi}$, modulation amplitude $\tilde{\Phi}$, frequency ω_p , and phase θ_p . An important special case occurs when the parking flux $\bar{\Phi}$ is set at a turning point in $\omega_T(\Phi)$, where the frequency modulation takes the approximate form

$$\omega_T(t) \approx \bar{\omega}_T(\tilde{\Phi}) + \tilde{\omega}_T(\tilde{\Phi}) \cos(2\omega_p t + 2\theta_p), \quad (2)$$

for $\tilde{\Phi} \lesssim \Phi_0/2$. The factors of 2 in Eq. (2) arise because, at these turning points, the transmon frequency undergoes two cycles for each cycle of the flux. The nonlinearity of $\omega_T(\Phi)$ results in the time-averaged frequency $\bar{\omega}_T$ being shifted away from $\omega_T(\bar{\Phi})$ by an amount that depends on $\tilde{\Phi}$. Our experimental results are obtained with the tunable transmon parked at $\bar{\Phi} = 0$, as depicted in Fig. 1(e). This condition offers first-order suppression of decoherence due to flux noise while idling [29].

The effect of the parametric modulation can be seen in an interaction frame defined by the instantaneous qubit frequencies. Indexing the two-transmon excited states as $|FT\rangle$ and approximating the (defined positive) transmon anharmonicities η_F and η_T as constant, we write the interaction Hamiltonian

$$\begin{aligned} \hat{H}_{\text{int}} = & g \sum_{n=-\infty}^{\infty} J_n \left(\frac{\tilde{\omega}_T}{2\omega_p} \right) e^{i(2n\omega_p t + \beta_n)} \\ & \times \{ e^{-i\Delta t} |10\rangle \langle 01| \\ & + \sqrt{2} e^{-i(\Delta + \eta_F)t} |20\rangle \langle 11| \\ & + \sqrt{2} e^{-i(\Delta - \eta_T)t} |11\rangle \langle 02| + \text{H.c.} \}, \quad (3) \end{aligned}$$

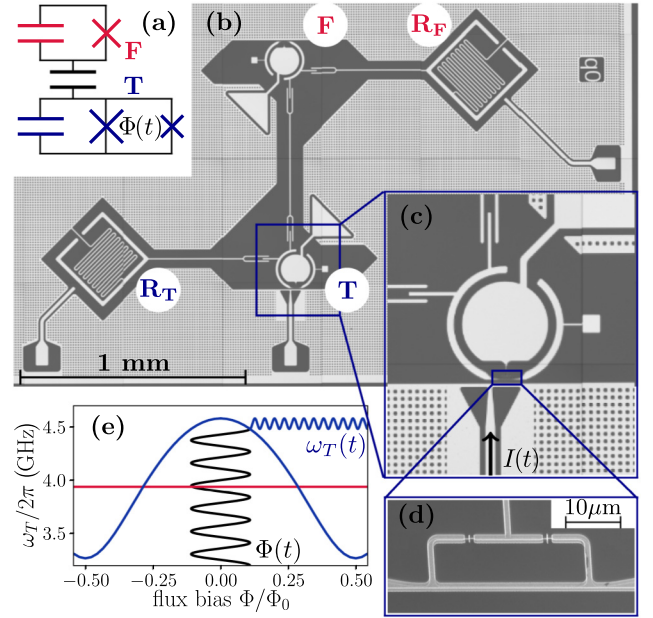


FIG. 1. Two-qubit circuit consisting of two capacitively coupled transmon qubits, one at fixed frequency (*F*) and one tunable (*T*). (a) Lumped-element circuit corresponding to our coupled qubits, where the tunable transmon is composed of an asymmetric SQUID with an asymmetry of 0.31. (b) Optical image of the chip. Lumped-element readout resonators are labeled R_F and R_T . (c) Time-varying flux pulses are actuated by a current $I(t)$ applied through the flux-bias line near *T*. (d) Scanning electron micrograph of the SQUID loop of the tunable transmon. (e) First transition frequency of the flux-tunable transmon (blue) and fixed-frequency transmon (red). Biasing the flux near the maximum or minimum of the band ensures long coherence times by removing first-order sensitivity to flux noise. The effect of flux modulation $\Phi(t)$ on the transmon frequency $\omega(t)$ is also shown in blue.

where J_n is the n th Bessel function of the first kind and where we denote the detuning and phase as

$$\Delta = \bar{\omega}_T(\tilde{\Phi}) - \omega_F, \quad (4)$$

$$\beta_n = (\tilde{\omega}_T/2\omega_p) \sin(2\theta_p) + (2\theta_p + \pi)n. \quad (5)$$

The interaction Hamiltonian makes plain the resonance conditions

$$2n\omega_p = \Delta(\tilde{\Phi}), \quad |10\rangle \leftrightarrow |01\rangle, \quad i\text{SWAP} \quad (6)$$

$$2n\omega_p = \Delta(\tilde{\Phi}) - \eta_T, \quad |11\rangle \leftrightarrow |02\rangle, \quad \text{CZ}_{02} \quad (7)$$

$$2n\omega_p = \Delta(\tilde{\Phi}) + \eta_F, \quad |11\rangle \leftrightarrow |20\rangle, \quad \text{CZ}_{20} \quad (8)$$

with harmonics $n = \pm 1, \pm 2, \pm 3, \dots$. These three types of entangling interactions are thus available at a series of amplitude-dependent modulation frequencies

corresponding to the level spacings in the driven two-qubit system. Each interaction has an effective coupling strength $g_{\text{eff}}^{(n)}$ that determines the Rabi frequency and resonant linewidth of the interaction at the n th harmonic. This is given by the time-independent prefactor of each term in the Hamiltonian, so that

$$g_{\text{eff}}^{(n)} = gJ_n \left(\frac{\tilde{\omega}_T}{2\omega_p} \right), \quad i\text{SWAP} \quad (9)$$

$$g_{\text{eff}}^{(n)} = \sqrt{2}gJ_n \left(\frac{\tilde{\omega}_T}{2\omega_p} \right), \quad \text{CZ}. \quad (10)$$

The flux drive introduces phase shifts β_n to the Hamiltonian, which depend on both the amplitude and phase of modulation. The Rabi frequency is maximal, and the gate time minimal, where J_n is maximal. For the first harmonic, this occurs for $\tilde{\omega}_T/2\omega_p \approx 1.84$, giving $J_1 \approx 0.582$.

The interaction Hamiltonian shown above is derived under a rotating-wave approximation, neglecting couplings between highly detuned levels. This approximation is valid for modulation frequencies $2\omega_p$ and couplings g well below the qubit frequencies. We also neglect the modulation of the anharmonicity and keep only the leading term in the coupling strengths between the different transitions. Taking these effects into account leads to small adjustments in the effective coupling rate for the range of modulation amplitudes used in this work. A more comprehensive analysis of this interaction is presented in Ref. [30].

A parametric drive that resonantly couples two levels produces swapping in the subspace of those levels, described by the unitary

$$\hat{U} = \begin{pmatrix} \cos(\theta/2) & -ie^{-i\phi} \sin(\theta/2) \\ -ie^{i\phi} \sin(\theta/2) & \cos(\theta/2) \end{pmatrix}, \quad (11)$$

with the population exchange given by $\theta = 2 \int_0^\tau g_{\text{eff}}(t) dt$ during the flux pulse, and the phase ϕ of the exchange given by β_n . The $i\text{SWAP}$ gate, mapping $\alpha |00\rangle + \beta |01\rangle + \gamma |10\rangle + \delta |11\rangle$ to $\alpha |00\rangle + i\gamma |01\rangle + i\beta |10\rangle + \delta |11\rangle$, is realized by selecting a modulation amplitude and frequency to satisfy the $i\text{SWAP}$ condition [Eq. (6)] and pulsing the modulation for a time τ that yields $\theta = \pi$. The CZ gates, mapping $\alpha |00\rangle + \beta |01\rangle + \gamma |10\rangle + \delta |11\rangle$ to $\alpha |00\rangle + \beta |01\rangle + \gamma |10\rangle - \delta |11\rangle$, are realized by activating one of the CZ resonances [Eqs. (7) and (8)] for a time that yields $\theta = 2\pi$. Physically, this causes the $|11\rangle$ state to fully leave and return to the computational basis, picking up the SU(2) phase of -1 in the process. Corrections of local phases, necessary to realize the correct unitary for each gate, are discussed below.

I. EXPERIMENTAL RESULTS

We implemented this proposal on a two-transmon device fabricated on a high-resistivity ($>10 \text{ k}\Omega \text{ cm}$) silicon substrate. In successive steps, Ti/Pd alignment marks and large Al features (ground planes, signal lines, and compact LC readout resonators) were defined using photolithography, electron-beam deposition, and liftoff. The transmon qubits, including Josephson junctions, were fabricated using the controlled undercut technique [31]. A bilayer resist stack consisting of methyl methacrylate (8.5) methacrylic acid copolymer and PMMA 950 was written with a 100-kV electron-beam lithography tool, and Al films were deposited in a Plassys MEB 550S at opposite substrate angles with an intervening controlled oxidation to form tunnel junctions.

The transmons were capacitively coupled to each other with a strength of $g/2\pi = 6.3 \text{ MHz}$, and to separate linear readout resonators with strengths of $\approx 70 \text{ MHz}$. The microwave XY control signals were delivered through the readout resonators, and the Z control of the tunable transmon was delivered on a single-ended on-chip flux-bias line. All RF signals used for qubit control and readout were transmitted (Tx) and received (Rx) by the Ettus Research USRP X300 software-defined radio platform, modified with custom gateway. A schematic of the experiment is given in Fig. 2. The tunable transmon frequencies were $\omega_T^{\text{max}}/2\pi = 4582$, $\eta_T^{\text{max}}/2\pi = 173$, $\omega_T^{\text{min}}/2\pi = 3285$, $\eta_T^{\text{min}}/2\pi = 185 \text{ MHz}$. The fixed transmon frequencies were $\omega_F/2\pi = 3940$ and $\eta_F/2\pi = 180 \text{ MHz}$.

The chip was operated with the tunable transmon parked at ω_T^{max} , where its relaxation and coherence times were $T_1 = 13$ and $T_2^* = 10 \mu\text{s}$. The fixed transmon had $T_1 = 34$ and $T_2^* = 20 \mu\text{s}$. Single-shot readout assignment fidelities of 0.85 (fixed) and 0.92 (tunable) were achieved

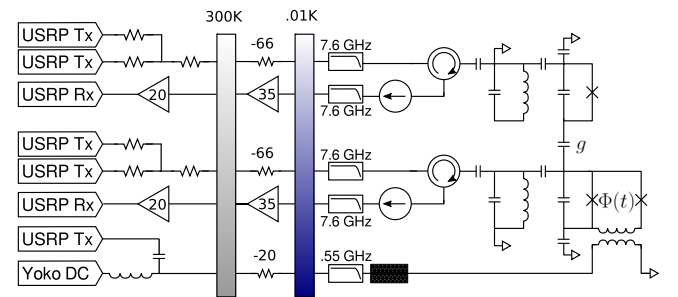


FIG. 2. Schematic of signal delivery to the two-qubit chip studied in this paper. Qubit drive and readout tones are transmitted, and the readout tone received, by Ettus Research USRP modules running with X300 daughterboards. The combined slow- and fast-flux components are generated by a Yokogawa GS200 dc power supply and another USRP X300, attenuated by 20 dB at 4 K and delivered through a UHF low-pass filter and a custom dissipative Eccosorb filter. The on-chip flux-bias line terminates in an inductive short to ground.

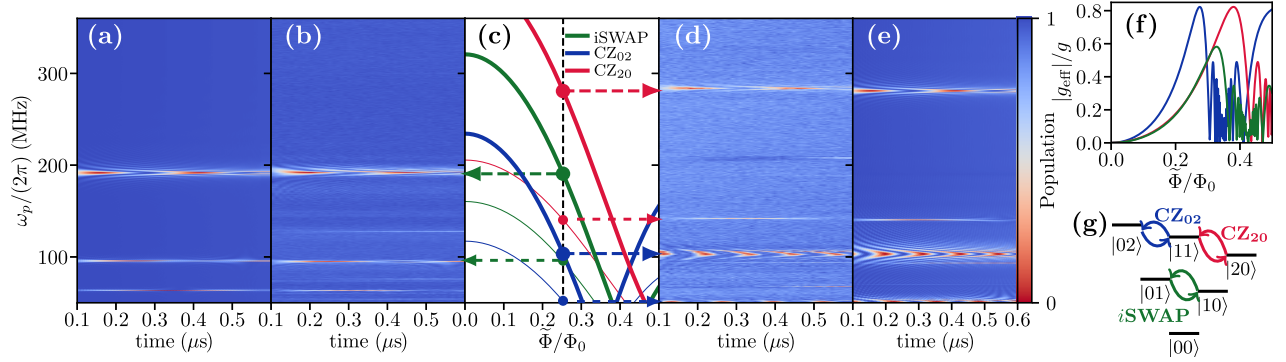


FIG. 3. Rabi oscillations driven by flux pulses. With a constant modulation amplitude and state preparation, we sweep pulse frequency and duration. The RF flux drive acts as a pump that compensates the energy detuning between two states. Rabi oscillations are observed when the modulation frequency matches the detuning between a pair of two-qubit states. (a),(b) With $|10\rangle$ prepared we observe $|10\rangle \leftrightarrow |01\rangle$ swapping, and (d),(e) with $|11\rangle$ prepared we observe both $|11\rangle \leftrightarrow |02\rangle$ and $|11\rangle \leftrightarrow |20\rangle$ swapping, by monitoring the population of the fixed transmon’s $|1\rangle$ state. The resonant frequencies depend on the modulation amplitude as shown in thick lines in (c), while the first harmonics of the resonances are shown in thin lines. These curves are the solutions of Eqs. (6)–(8) for $n = 1, 2$ and thus reflect the form of $\Delta(\tilde{\Phi})$. This function is calculated using the transmon energies extracted from frequency measurements. Further details on this calculation are available in Ref. [30]. Together these plots show a concordance of theory (c), dynamical simulations (a),(e), and data (b),(d) obtained with a modulation amplitude of $0.245\Phi_0$. Higher harmonics are also visible in this concordance, but they are left unlabeled for clarity. In (f) we show the effective coupling strength g_{eff} as a function of modulation amplitude for the first harmonic of each interaction [following the same color scheme as in (c),(g)], and in (g) we show the energy-level diagram of the two-qubit system.

using dispersive readouts combined with a binary classifier trained on $|0\rangle$ and $|1\rangle$ state preparation for each qubit [32]. This classifier was used to categorize the simultaneous readout signals obtained in the two-qubit tomography and randomized benchmarking results described below. Single-qubit randomized benchmarking decay constants of greater than 0.98 were obtained. Application of the flux modulation increased the tunable transmon’s sensitivity to flux noise, such that we measured $T_2^* \approx 4 \mu\text{s}$ with the drive applied. In principle the flux modulation may also increase the qubit’s relaxation rate [15,33], but we found that T_1 was consistent with the flux drive on versus off.

As illustrated in Fig. 3, we observed the resonance conditions for the *i*SWAP and CZ interactions as predicted by theory and numerical simulations. Our simulations were performed by evolving the Lindblad master equation with the full Hamiltonian of the circuit-QED system under flux modulation. The master equation included dephasing and dissipation consistent with the measured values of T_1 and T_2^* under modulation, reported in Table I. To obtain this concordance we measured the transfer function of flux pulses to the tunable transmon by measuring the average qubit frequency $\bar{\omega}_T$ during modulation, as a function of both amplitude and frequency over the nominal 0–500-MHz passband of the signal chain. For data collection we then applied a frequency-dependent amplitude correction, similar to [26], to flatten the frequency response.

Closer inspection of the resonant features also showed good agreement between theory and observations of a characteristic “chevron” signal (see Fig. 4). This signal was used to confirm the resonant frequency at the chosen

value of modulation amplitude. The parametric *i*SWAP and CZ gates were then realized by determining which pulse durations τ yielded the appropriate values of θ .

Once a fully entangling interaction is specified, realizing the desired unitary for each gate requires a number of corrections to be applied.

- (1) The mean qubit frequencies are shifted during the modulation and thus acquire local phases with respect to

TABLE I. Summary of experimental results. The operating point for each gate is given by the flux-modulation amplitude and frequency. The gate durations and g_{eff} values include the pulse risetimes of 30–40 ns. The values of T_1 and T_2^* are estimated under drive conditions by measuring the decay of the qubit as a function of flux-pulse duration. Fidelities are given using both process tomography and randomized benchmarking, with accompanying bounds on the tomography result. Further detail on the fidelity characterization is provided in the main text.

| Gate | <i>i</i> SWAP | CZ ₀₂ | CZ ₂₀ |
|-------------------------------------|---------------|------------------|------------------|
| $\tilde{\Phi}$ (units of Φ_0) | 0.317 | 0.245 | 0.280 |
| $\omega_p/2\pi$ (MHz) | 122 | 112 | 253 |
| Duration (ns) | 150 | 210 | 290 |
| $g_{\text{eff}}/2\pi$ (MHz) | 3.9 | 4.0 | 2.4 |
| Effective T_1 (μs) | 5–25 | 7–17 | 7–17 |
| Effective T_2^* (μs) | 4.6(8) | 10.2(22) | 7.1(11) |
| IRB fidelity | 0.94 | 0.92 | 0.91 |
| Clifford fidelity | 0.94 | 0.93 | 0.88 |
| QPT fidelity | 0.93 | 0.92 | 0.92 |
| Unitarity bound | 0.939 | 0.945 | 0.935 |
| Interferometric bound | 0.938 | 0.945 | 0.935 |

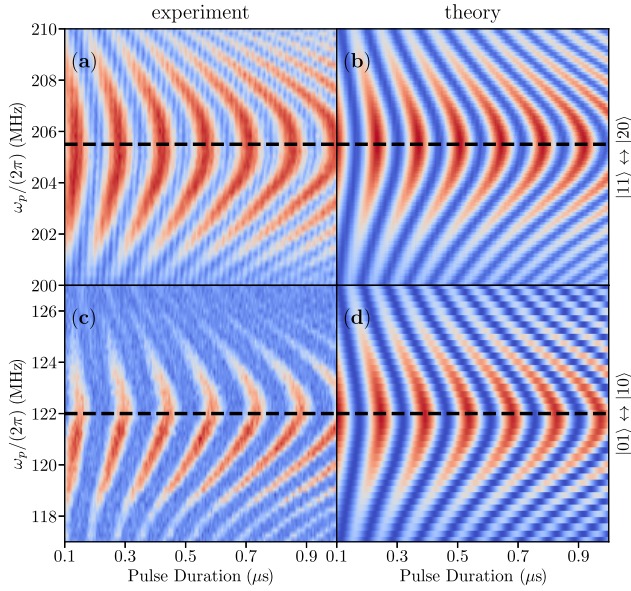


FIG. 4. Enlarged view of resonant features, similar to those shown in Fig. 3, reveals a “chevron” pattern characteristic of Rabi oscillations. For each type of gate, a modulation amplitude is chosen to provide a suitable g_{eff} . With that amplitude held constant, the flux-pulse duration and frequency are varied and values are chosen to give the roughly the desired gate up to local phases. The patterns observed in the experimental data (left) are in good agreement with the predictions of a dynamical simulation (right), as shown here for transitions $|01\rangle \leftrightarrow |10\rangle$ at $\tilde{\Phi} = 0.318 \Phi_0$ (bottom) and $|11\rangle \leftrightarrow |20\rangle$ at $\tilde{\Phi} = 0.325 \Phi_0$ (top). The only free parameters in the model are the effective relaxation and coherence times in the presence of flux drives.

their microwave drives. These local phases were measured with a Ramsey experiment where only the phase of the second $\pi/2$ pulse was varied. The corrections for the phases were then implemented as local updates to the phases of downstream microwave pulses. The mean shifts depend in general on the initial phase of each flux pulse; however, this effect can be suppressed by using risetimes much slower than the modulation frequency. For this reason we used risetimes of 30–40 ns.

(2) The frequency of the flux pulse must be chosen according to the resonant condition [Eq. (4)], which is affected by the shifts in qubit frequencies. However, when the flux pulse is not applied, the dynamical phase between the two levels accumulates at the unshifted detuning of the two levels. Because the flux pulses were generated using a local oscillator tuned to the shifted frequency, the phases of successive pulses required correction for the mean shift of the qubit frequencies.

(3) The phase β_n is present in the i SWAP interaction, where the off-diagonal elements of Eq. (11) are nonzero, and is set by the phase θ_p of flux modulation with respect to the individual qubit frames. This interaction phase can be handled either by updating the phase of the flux drive or

pushed to equal and opposite local frame changes applied after the gate.

(4) The exchange of states in the i SWAP gate entails the exchange of their local phases. This was tracked by swapping the microwave phases after each i SWAP gate.

Characteristics of each gate are given in Table I. The average gate fidelity of each operation was estimated using interleaved randomized benchmarking (IRB) [34,35] as well as maximum-likelihood quantum process tomography (QPT) [36]. In using QPT to estimate the gate fidelities [37,38] we compensated for the known readout infidelities [32,39] and applied complete-positivity (CP) constraints. We estimate $F_{i\text{SWAP}} = 0.93$ and $F_{\text{CZ}} = 0.92$ for both the CZ₀₂ and CZ₂₀ gates. The constrained reconstructions, along with the ideal target gates, are depicted in Fig. 5. Similar devices have also yielded average fidelities for CZ gate above 0.9 [32]. The result of the IRB experiment for the i SWAP gate is shown in Fig. 6.

In order to roughly identify the source of the observed infidelities, we estimate the fidelity to the unitary closest to the reconstructed evolution. If the fidelity to the closest unitary is similar to the fidelity to the ideal target gate, we conclude there were no significant coherent errors, and that the fidelity is limited by the decoherence of the evolution. Otherwise, we conclude there are significant coherent errors in the evolutions. There are two natural notions of closest unitary for a reconstructed superoperator \mathcal{E} with corresponding canonical Kraus representation $\mathcal{E}(\rho) = \sum_i K_i \rho K_i^\dagger$ [40] and with Liouville representation singular value decomposition $\mathcal{E} = \mathcal{U}\mathcal{S}\mathcal{V}^\dagger$. One is given by the unitary U_0 where $\|K_0\| \geq \|K_{i>0}\|$, and where $K_0 = U_0 P_0$ is a polar decomposition [41], which results in the approximate interferometric bound

$$\bar{F} \gtrsim \frac{\text{tr}(U_0^* \otimes U_0)^\dagger \mathcal{E} + d}{d^2 + d}, \quad (12)$$

where $d = 4$ is the dimension of the Hilbert space of interest. The other is given by $\mathcal{U}\mathcal{V}^\dagger$, which results in the strict Procrustean unitarity bound

$$\bar{F} \leq \frac{\text{tr} \mathcal{S} + d}{d^2 + d}. \quad (13)$$

These upper bounds are consistent with our measured fidelity estimates, indicating that infidelities are largely explained by the decoherence during the gate evolution.

II. SUMMARY

We propose and demonstrate parametric i SWAP and CZ gates activated by modulating the frequency of a tunable transmon. We show close agreement between observed and predicted resonance conditions over a wide range of frequencies and multiple drive amplitudes, and we

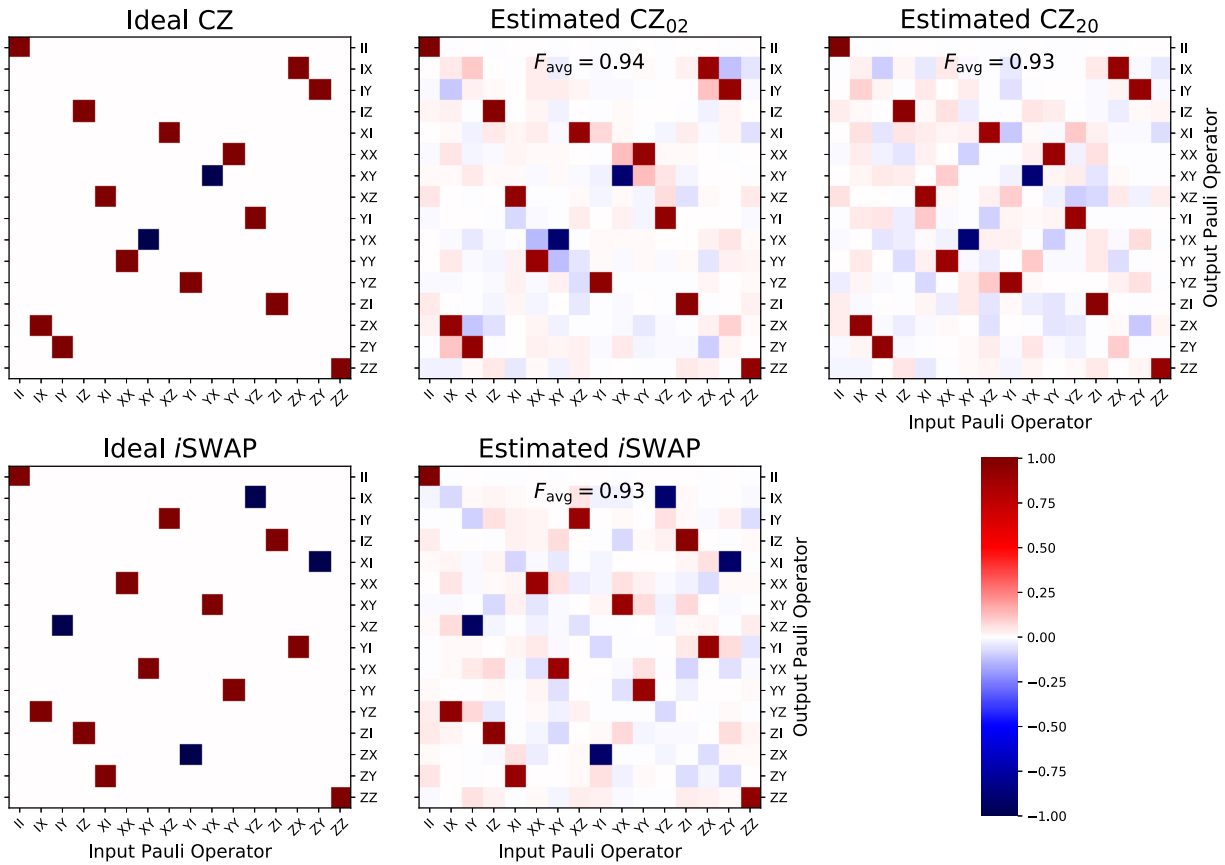


FIG. 5. Two-qubit process tomography parametric CZ (top) and *i*SWAP (bottom) processes. The corresponding average process fidelities are $F = 0.92$ for both CZ processes and $F = 0.93$ for the *i*SWAP process.

describe and implement local phase corrections necessary to produce correct and repeatable unitaries. Gate fidelities, estimated by interleaved randomized benchmarking and quantum process tomography, are estimated to be

0.91–0.94 and appear to be limited by decoherence during the parametric drive. The underlying interactions used in this technique are highly selective and provide a way to mitigate frequency crowding in a scalable quantum processor architecture.

ACKNOWLEDGMENTS

Part of this work was performed at the Stanford Nano Shared Facilities (SNSF), supported by the National Science Foundation under Grant No. ECCS-1542152.

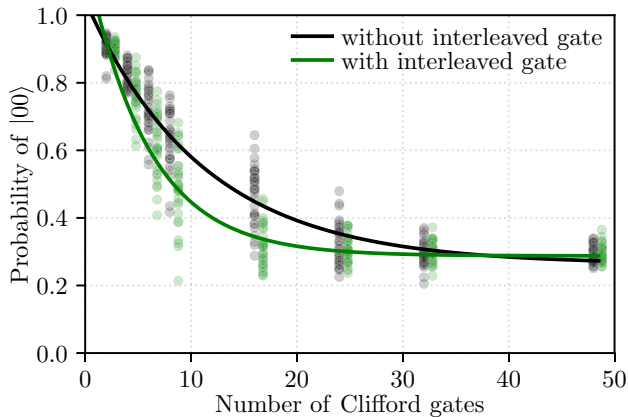


FIG. 6. Interleaved randomized benchmarking result for the *i*SWAP gate. In this experiment, sequence lengths of {2, 4, 6, 8, 16, 24, 32, 48} are used. For visual clarity, the data points for each sequence length are offset symmetrically about the true length. The fit curves, however, are not offset. The accelerated decay from the expected final state of $|00\rangle$ is attributed to the error in the *i*SWAP gate.

[1] J. Koch, T. M. Yu, J. Gambetta, A. A. Houck, D. I. Schuster, J. Majer, A. Blais, M. H. Devoret, S. M. Girvin, and R. J. Schoelkopf, Charge-insensitive qubit design derived from the cooper pair box, *Phys. Rev. A* **76**, 042319 (2007).

[2] A. Blais, J. Gambetta, A. Wallraff, D. I. Schuster, S. M. Girvin, M. H. Devoret, and R. J. Schoelkopf, Quantum-information processing with circuit quantum electrodynamics, *Phys. Rev. A* **75**, 032329 (2007).

[3] C. Rigetti, and M. Devoret, Fully microwave-tunable universal gates in superconducting qubits with linear couplings and fixed transition frequencies, *Phys. Rev. B* **81**, 134507 (2010).

- [4] C. Rigetti, A. Blais, and M. Devoret, Protocol for Universal Gates in Optimally Biased Superconducting Qubits, *Phys. Rev. Lett.* **94**, 240502 (2005).
- [5] J. M. Chow, A. D. Córcoles, J. M. Gambetta, C. Rigetti, B. R. Johnson, John A. Smolin, J. R. Rozen, G. A. Keefe, M. B. Rothwell, M. B. Ketchen, and M. Steffen, Simple All-Microwave Entangling Gate for Fixed-Frequency Superconducting Qubits, *Phys. Rev. Lett.* **107**, 080502 (2011).
- [6] P. J. Leek, S. Filipp, P. Maurer, M. Baur, R. Bianchetti, J. M. Fink, M. Göppl, L. Steffen, and A. Wallraff, Using sideband transitions for two-qubit operations in superconducting circuits, *Phys. Rev. B* **79**, 180511 (2009).
- [7] S. Poletto, J. M. Gambetta, S. T. Merkel, J. A. Smolin, J. M. Chow, A. D. Córcoles, G. A. Keefe, M. B. Rothwell, J. R. Rozen, D. W. Abraham, C. Rigetti, and M. Steffen, Entanglement of Two Superconducting Qubits in a Waveguide Cavity via Monochromatic Two-Photon Excitation, *Phys. Rev. Lett.* **109**, 240505 (2012).
- [8] S. Sheldon, E. Magesan, J. M. Chow, and J. M. Gambetta, Procedure for systematically tuning up cross-talk in the cross-resonance gate, *Phys. Rev. A* **93**, 060302 (2016).
- [9] M. D. Hutchings, Jared B. Hertzberg, Yebin Liu, Nicholas T. Bronn, George A. Keefe, Jerry M. Chow, and B. L. T. Plourde, Tunable superconducting qubits with flux-independent coherence, arXiv:1702.02253.
- [10] F. W. Strauch, Quantum logic gates for superconducting resonator qubits, *Phys. Rev. A* **84**, 052313 (2011).
- [11] L. DiCarlo, J. M. Chow, J. M. Gambetta, L. S. Bishop, B. R. Johnson, D. I. Schuster, J. Majer, A. Blais, L. Frunzio, S. M. Girvin, and R. J. Schoelkopf, Demonstration of two-qubit algorithms with a superconducting quantum processor, *Nature* **460**, 240 (2009).
- [12] T. Yamamoto, M. Neeley, E. Lucero, R. C. Bialczak, J. Kelly, M. Lenander, Matteo Mariantoni, A. D. O'Connell, D. Sank, H. Wang, M. Weides, J. Wenner, Y. Yin, A. N. Cleland, John M. Martinis, Quantum process tomography of two-qubit controlled-z and controlled-not gates using superconducting phase qubits, *Phys. Rev. B* **82**, 184515 (2010).
- [13] J. Kelly, R. Barends, A. G. Fowler, A. Megrant, E. Jeffrey, T. C. White, D. Sank, J. Y. Mutus, B. Campbell, Yu Chen, Z. Chen, B. Chiaro, A. Dunsworth, I.-C. Hoi, C. Neill, P. J. J. O'Malley, C. Quintana, P. Roushan, A. Vainsencher, J. Wenner, A. N. Cleland, and J. M. Martinis, State preservation by repetitive error detection in a superconducting quantum circuit, *Nature* **519**, 66 (2015).
- [14] Mathew Reed, Ph.D. thesis, Yale.
- [15] J. Kelly, R. Barends, A. G. Fowler, A. Megrant, E. Jeffrey, T. C. White, D. Sank, J. Y. Mutus, B. Campbell, Yu Chen, Z. Chen, B. Chiaro, A. Dunsworth, I.-C. Hoi, C. Neill, P. J. J. O'Malley, C. Quintana, P. Roushan, A. Vainsencher, J. Wenner, A. N. Cleland, and J. M. Martinis, State preservation by repetitive error detection in a superconducting quantum circuit, *Nature* **519**, 66 (2015).
- [16] E. A. Sete, W. J. Zeng, and C. T. Rigetti, in *2016 IEEE International Conference on Rebooting Computing (ICRC)* (IEEE, 2016).
- [17] A. J. Kerman, and W. D. Oliver, High-Fidelity Quantum Operations on Superconducting Qubits in the Presence of Noise, *Phys. Rev. Lett.* **101**, 070501 (2008).
- [18] P. Bertet, C. J. P. M. Harmans, and J. E. Mooij, Parametric coupling for superconducting qubits, *Phys. Rev. B* **73**, 064512 (2006).
- [19] A. O. Niskanen, Y. Nakamura, and J. S. Tsai, Tunable coupling scheme for flux qubits at the optimal point, *Phys. Rev. B Condens. Matter Mater. Phys.* **73**, 1 (2006), arXiv:0512238 [cond-mat].
- [20] A. O. Niskanen, K. Harrabi, F. Yoshihara, Y. Nakamura, S. Lloyd, and J. S. Tsai, Quantum coherent tunable coupling of superconducting qubits, *Science (New York, N.Y.)* **316**, 723 (2007).
- [21] F. Beaudoin, M. P. da Silva, Z. Dutton, and A. Blais, First-order sidebands in circuit qed using qubit frequency modulation, *Phys. Rev. A* **86**, 022305 (2012).
- [22] J. D. Strand, M. Ware, F. Beaudoin, T. A. Ohki, B. R. Johnson, A. Blais, and B. L. T. Plourde, First-order sideband transitions with flux-driven asymmetric transmon qubits, *Phys. Rev. B* **87**, 220505 (2013).
- [23] B. Royer, A. L. Grimsmo, N. Didier, and A. Blais, Fast and high-fidelity entangling gate through parametrically modulated longitudinal coupling, *Quantum* **1**, 11 (2017).
- [24] T. Roy, S. Kundu, M. Chand, S. Hazra, N. Nehra, R. Cosmic, A. Ranadive, M. P. Patankar, K. Damle, and R. Vijay, Implementation of Pairwise Longitudinal Coupling in a Three-Qubit Superconducting Circuit, *Phys. Rev. Appl.* **7**, 054025 (2017).
- [25] D. C. McKay, S. Filipp, A. Mezzacapo, E. Magesan, J. M. Chow, and J. M. Gambetta, Universal Gate for Fixed-Frequency Qubits via a Tunable Bus, *Phys. Rev. Appl.* **6**, 064007 (2016).
- [26] R. K. Naik, N. Leung, S. Chakram, P. Groszkowski, Y. Lu, N. Earnest, D. C. McKay, J. Koch, and D. I. Schuster, Random access quantum information processors, arXiv:1705.00579.
- [27] N. Schuch, and J. Siewert, Natural two-qubit gate for quantum computation using the XY interaction, *Phys. Rev. A* **67**, 032301 (2003).
- [28] A. Barenco, C. H. Bennett, R. Cleve, D. P. DiVincenzo, N. Margolus, P. Shor, T. Sleator, J. A. Smolin, and H. Weinfurter, Elementary gates for quantum computation, *Phys. Rev. A* **52**, 3457 (1995).
- [29] D. Vion, A. Aassime, A. Cottet, P. Joyez, H. Pothier, C. Urbina, D. Esteve, and M. H. Devoret, Manipulating the quantum state of an electrical circuit, *Science* **296**, 886 (2002).
- [30] Nicolas Didier, Eyob A. Sete, Marcus P. da Silva, and Chad Rigetti, Analytical modeling of parametrically modulated transmon qubits, *Phys. Rev. A* **97**, 022330 (2018).
- [31] F. Lecocq, I. M. Pop, Z. Peng, I. Matei, T. Crozes, T. Fournier, C. Naud, W. Guichard, and O. Buisson, Junction fabrication by shadow evaporation without a suspended bridge, *Nanotechnology* **22**, 315302 (2011).
- [32] Matthew Reagor, Christopher B. Osborn, Nikolas Tezak, Alexa Staley, Guenevere Prawiroatmodjo, Michael Scheer, Nasser Alidoust, Eyob A. Sete, Nicolas Didier, Marcus P. da Silva, Ezer Acala, Joel Angeles, Andrew Bestwick, Maxwell Block, Benjamin Bloom, Adam Bradley, Catvu Bui, Shane Caldwell, Lauren Capelluto, Rick Chilcott, Jeff Cordova, Genya Crossman, Michael Curtis, Saniya Deshpande, Tristan El Bouayadi, Daniel Girshovich, Sabrina Hong, Alex Hudson, Peter Karalekas, Kat Kuang,

- Michael Lenihan, Riccardo Manenti, Thomas Manning, Jayss Marshall, Yuvraj Mohan, William O'Brien, Johannes Otterbach, Alexander Papageorge, Jean-Philip Paquette, Michael Pelstring, Anthony Polloreno, Vijay Rawat, Colm A. Ryan, Russ Renzas, Nick Rubin, Damon Russel, Michael Rust, Diego Scarabelli, Michael Selvanayagam, Rodney Sinclair, Robert Smith, Mark Suska, Ting-Wai To, Mehrnoosh Vahidpour, Nagesh Vodrahalli, Tyler Whyland, Kamal Yadav, William Zeng, and Chad T. Rigetti, Demonstration of universal parametric entangling gates on a multi-qubit lattice, *Sci. Adv.* **4**, eaao3603 (2018). <http://advances.sciencemag.org/content/4/2/eaao3603.full.pdf>.
- [33] J. M. Martinis, K. B. Cooper, R. McDermott, M. Steffen, M. Ansmann, K. D. Osborn, K. Cicak, S. Oh, D. P. Pappas, R. W. Simmonds, Clare C. Yu, Decoherence in Josephson Qubits from Dielectric Loss, *Phys. Rev. Lett.* **95**, 210503 (2005).
- [34] J. P. Gaebler, A. M. Meier, T. R. Tan, R. Bowler, Y. Lin, D. Hanneke, J. D. Jost, J. P. Home, E. Knill, D. Leibfried, and D. J. Wineland, Randomized Benchmarking of Multiqubit Gates, *Phys. Rev. Lett.* **108**, 260503 (2012).
- [35] Easwar Magesan, Jay M. Gambetta, Blake R. Johnson, Colm A. Ryan, Jerry M. Chow, Seth T. Merkel, Marcus P. da Silva, George A. Keefe, Mary B. Rothwell, Thomas A. Ohki, *et al.*, Efficient Measurement of Quantum Gate Error by Interleaved Randomized Benchmarking, *Phys. Rev. Lett.* **109**, 080505 (2012).
- [36] Z. Hradil, J. Řeháček, J. Fiurášek, and M. Ježek, in Quantum State Estimation (Springer, 2004), pp. 59–112.
- [37] M. Horodecki, P. Horodecki, and R. Horodecki, General teleportation channel, singlet fraction, and quasidistillation, *Phys. Rev. A* **60**, 1888 (1999).
- [38] M. A. Nielsen, A simple formula for the average gate fidelity of a quantum dynamical operation, *Phys. Lett. A* **303**, 249 (2002).
- [39] Colm A. Ryan, Blake R. Johnson, Jay M. Gambetta, Jerry M. Chow, Marcus P. da Silva, Oliver E. Dial, and Thomas A. Ohki, Tomography via correlation of noisy measurement records, *Phys. Rev. A* **91**, 022118 (2015).
- [40] Timothy F. Havel, Robust procedures for converting among Lindblad, Kraus and matrix representations of quantum dynamical semigroups, *J. Math. Phys.* **44**, 534 (2003).
- [41] D. K. L. Oi, Interference of Quantum Channels, *Phys. Rev. Lett.* **91**, 067902 (2003).